# Synthesis and characterization of ruthenium dioxide nanostructures

S. Neupane · G. Kaganas · R. Valenzuela ·
L. Kumari · X. W. Wang · W. Z. Li

**Abstract** We report the synthesis of ruthenium dioxide ($RuO_2$) nanostructures by thermal evaporation of $RuO_2$ powder. $RuO_2$ nanostructures of different shapes were synthesized at various concentration, flow rate, and pressure of oxygen. At a constant pressure of 3 torr of flowing oxygen, polygonal prism-like $RuO_2$ nanorods with flat tips were grown at an $O_2$ flow rate of 100 sccm; club-shaped nanorods with obelisk tip were formed at 300 and 600 sccm, and hollow rods with square tip were formed at 1800 sccm. A mixture of $O_2$ and Ar at a total flow rate of 600 sccm led to the formation of short club-shaped nanorods indicating the suppression effect of Ar on the growth of nanorods. The pressure also had a significant effect on the formation of $RuO_2$ nanostructures, at a fixed flow rate of 600 sccm of $O_2$, a pressure of 3 torr resulted in the growth of club-shaped $RuO_2$ nanorods, while high pressures of 380 and 760 torr resulted in the formation of both linear club-shaped and pine tree-like hierarchical $RuO_2$ nanorods. X-ray diffraction and transmission electron microscopy analysis indicated the formation of tetragonal phase of $RuO_2$ with high crystallinity. A density functional calculation on $RuO_2$, $RuO_3$, and $RuO_4$ was performed to help to explain the experimental results.

S. Neupane · G. Kaganas · R. Valenzuela · L. Kumari ·
X. W. Wang (✉) · W. Z. Li (✉)
Department of Physics, Florida International University,
Miami, FL 33199, USA
e-mail: sherwin@fiu.edu

W. Z. Li
e-mail: Wenzhi.Li@fiu.edu

## Introduction

One-dimensional nanostructures exhibit significantly different properties as compared to their bulk counterparts and have garnered great interest due to their wide range of applications. Ruthenium dioxide ($RuO_2$) nanorods hold a promising future in nanoelectronics application. $RuO_2$, a rutile-type tetragonal oxide [1], exhibits low resistivity ($\sim 35\mu\Omega$ cm) at room temperature [2] and is thermally and chemically stable over a wide temperature range [3]. $RuO_2$ films are used as resistors [4, 5], electrode for supercapacitors [6, 7], fatigue resistant ferroelectric RAM, and dynamic random access memory [8, 9]. $RuO_2$ is also used as anode coating for chlorine and oxygen production [10–12] and to provide electronic path in silica aerogels [13]. $RuO_2$ nanorods are good candidates for field emission [14] and charge storage materials [15].

Several synthesis methods have been employed to produce $RuO_2$ in different forms. $RuO_2$ crystals have been grown from the decomposition of volatile oxides of Ru [2]. Thin films of $RuO_2$ have been produced by chemical vapor deposition (CVD) of organic compounds of Ru [3], pulsed laser deposition of pure $RuO_2$ target [16], and electrostatic spray deposition of $RuCl_3$ [6, 17]. $RuO_2$ nanorods have been synthesized by reducing $RuCl_3$ over carbon nanotube templates [18], reactive sputtering of pure Ru in the $O_2$ environment [19], and CVD of Ru containing compounds with $O_2$ as carrier gas [20]. Thermal decomposition of Ru containing compounds in a continuous flow of carrier gas has also resulted in the growth of $RuO_2$ nanorods [21].

In this study, we report the growth of $RuO_2$ nanostructures by thermal evaporation method under different synthesis conditions which results in good control over morphology, crystallinity, and purity of the nanostructures. The experiments are carried out to study the formation of

various $RuO_2$ nanostructures at different $O_2$ flow rates, variable ratios of $O_2$ to Ar, and different pressures. The crystal structure and surface morphology of the as-grown $RuO_2$ nanostructures were also investigated. An electronic structure calculation on $RuO_2$, $RuO_3$, and $RuO_4$ was performed to elucidate the synthesis mechanism of the $RuO_2$ nanostructures.

## Experimental

The $RuO_2$ nanostructures were synthesized by thermal evaporation method. Analytic grade anhydrous Ruthenium (IV) oxide (99.5%) was used as the precursor material. The precursor material was heated to 1000 °C in a quartz boat inside a quartz tube placed at the center of a tube furnace. A silicon (100) wafer sputtered with gold for 15 s was used as the substrate and placed at 350 °C in the downstream flow of the reaction vapor. $RuO_2$ nanostructures were grown on the Si substrate using the gold as catalyst at various flow rates and pressures of $O_2$ or mixture of $O_2/Ar$. The Si substrate was placed at a distance of 22 cm from the quartz boat, and the average thickness of the gold coating on the Si substrate was 2.5 nm. The pressure inside the quartz tube was maintained using a mechanical pump. Experiments were carried out at $O_2$ flow rates of 100, 300, 600, and 1800 sccm, respectively, with a fixed pressure of 3 torr and a growth time of 5 h to study the effect of $O_2$ flow rate on the morphology of the $RuO_2$ nanostructures. To investigate the influence of the gas pressure on the formation of the $RuO_2$ nanostructures, the synthesis was also performed at working pressures of 3, 380, and 760 torr at a fixed $O_2$ flow of 600 sccm. Experiments were also done using 5, 10, and 25% of $O_2$ in Ar at an overall flow rate of 600 sccm and working pressure of 3 torr to understand the effect of $O_2$ concentration on the growth of the $RuO_2$ nanostructures.

Structural analysis of the synthesized $RuO_2$ nanostructures was carried out using an X-ray diffractometer (XRD, D-8 Bruker–AXS) equipped with Cu Kα radiation source ($\lambda = 1.5406$ Å) and a two-dimensional area detector. Surface morphology analysis of the $RuO_2$ nanostructures was performed by a field emission scanning electron microscope (SEM, JEOL JSM-6330F) operated at an accelerating voltage of 15 kV. Transmission electron microscopy (TEM) images, high resolution TEM (HRTEM) images and selected-area electron diffraction (SAED) patterns were obtained from a JEOL-2010F apparatus operated at an accelerating voltage of 200 kV. For the TEM analysis, the $RuO_2$ material synthesized on the Si substrate was removed and dispersed ultrasonically in ethanol and the solution was dropped on the carbon coated copper TEM grid.

## Results and discussion

Crystal structure analysis by X-ray diffraction

Figure 1a and b displays the typical XRD patterns of the $RuO_2$ nanostructures synthesized at the oxygen flow rates of 300 sccm (see the corresponding SEM images in Fig. 3a, b) and 600 sccm (see the corresponding SEM images in Fig. 3c, d), respectively. For the two samples examined by XRD in Fig. 1, the synthesis time was 5 h, and the working pressure was 3 torr. All diffraction peaks observed in the Fig. 1 can be indexed to the rutile $RuO_2$ with tetragonal phase which is in agreement with the standard data (JCPDS 88-0322). The presence of sharp peaks of rutile $RuO_2$ and the absence of any peaks corresponding to other phases of $RuO_2$ indicate the high purity and crystallinity of the as-synthesized $RuO_2$ structures. XRD profiles in Fig. 1a and 1b show a predominant contribution from [110] plane. The lattice parameters for tetragonal $RuO_2$ are $a = b = 0.449$ nm and $c = 0.311$ nm and for Si are $a = b = c = 0.543$. The lattice mismatch at the interface between the $RuO_2$ and the Si substrate produces strain energy when $RuO_2$ is nucleated. The growth direction which minimizes the lattice mismatch and produces the minimum strain energy is the most preferential growth direction. For rutile structured materials, the most thermodynamically stable surface is the (110) face [22]. Hence, nanorods are expected to grow with the preferred orientation along (110) direction under equilibrium condition. At non-equilibrium condition, the synthesis of
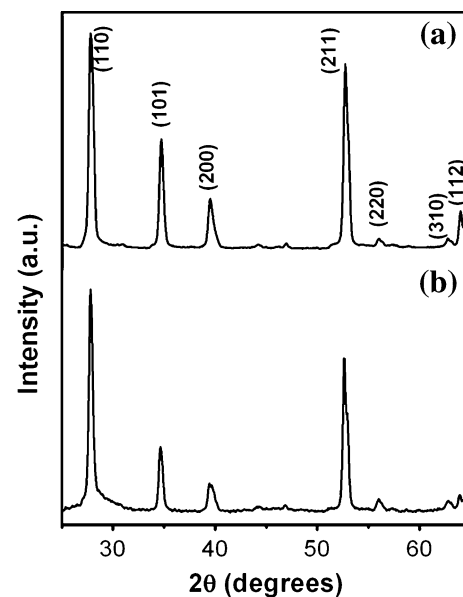


**Fig. 1** XRD patterns of club-like $RuO_2$ nanostructures synthesized under the working pressure of 3 torr and at $O_2$ flow rates of **a** 300 sccm and **b** 600 sccm, respectively

nanorods is favored along more closely spaced growth planes. The (101) plane is the next densest plane compared to the (110) face and is the preferred growth direction under such condition. From the XRD analysis, it can be concluded that the $RuO_2$ nanorods show a crystal structure with preferential crystalline alignment along the [001] direction indicating the crystal growth along the *c*-axis. The XRD profiles of remaining samples synthesized under other conditions also exhibited the similar pattern.

## Morphology analysis by scanning electron microscopy

### Effect of oxygen flow rate

Figure 2 shows the surface morphology of the $RuO_2$ nanorods synthesized at 1000 °C for 5 h, and the pressure inside the reaction tube was maintained at 3 torr with the $O_2$ flow rate of 100 sccm. The low-magnification image in Fig. 2a represents the large-scale growth of $RuO_2$ nanorods, which form a uniform layer on the surface of the Si substrate. The high-magnification SEM image in Fig. 2b shows that the nanorods are polygonal prisms with flat tips. It can be observed that the $RuO_2$ nanorods grow out from the surface of the Si substrate and the nanorods have an average length of 15 μm and width of about 400–1000 nm.

The top and cross-sectional views of the $RuO_2$ nanostructures synthesized at $O_2$ flow rates of 300, 600, and 1800 sccm are shown in Fig. 3a, b, c, d, e, and f, respectively. For these experiments, the temperature was maintained at 1000 °C, the pressure inside the reaction chamber was kept at 3 torr, and the growth time was set for 5 h. The SEM results show that vertically aligned high density club-like submicron-sized rods are formed at $O_2$ flow rates of 300 and 600 sccm (Fig. 3a, b, c, and d). The rods synthesized at $O_2$ flow rate of 300 sccm have an average width of 1.8 μm and length of around 21 μm (Fig. 3b). The club-like rods synthesized at the $O_2$ flow rate of 600 sccm are about 1 μm wide and 10 μm long (Fig. 3d). These club-like rods taper towards the bottom and their tips have an obelisk structure as compared to the uniform polygonal prism-like nanorods with a flat tip synthesized with the $O_2$ flow rate of 100 sccm (see Fig. 2a). The SEM images in Fig. 3e, f show high density of submicron-size $RuO_2$ hollow rods synthesized at the $O_2$ flow rate of 1800 sccm. These hollow rods have a square cross section with an average width of 1.8 μm at the top and are about 8 μm tall. These hollow rods taper towards the bottom and widen significantly at the top. There is a substantial decrease in the length of the $RuO_2$ rods as the $O_2$ flow rate increases from 300 to 1800 sccm. The densities of the $RuO_2$ rods formed at different $O_2$ flow rates of 100, 300, 600, and 1800 sccm are $2.4 \times 10^7$ cm$^{-2}$, $4.7 \times 10^8$ cm$^{-2}$, $1.4 \times 10^6$ cm$^{-2}$, and $1.0 \times 10^7$ cm$^{-2}$, respectively. A
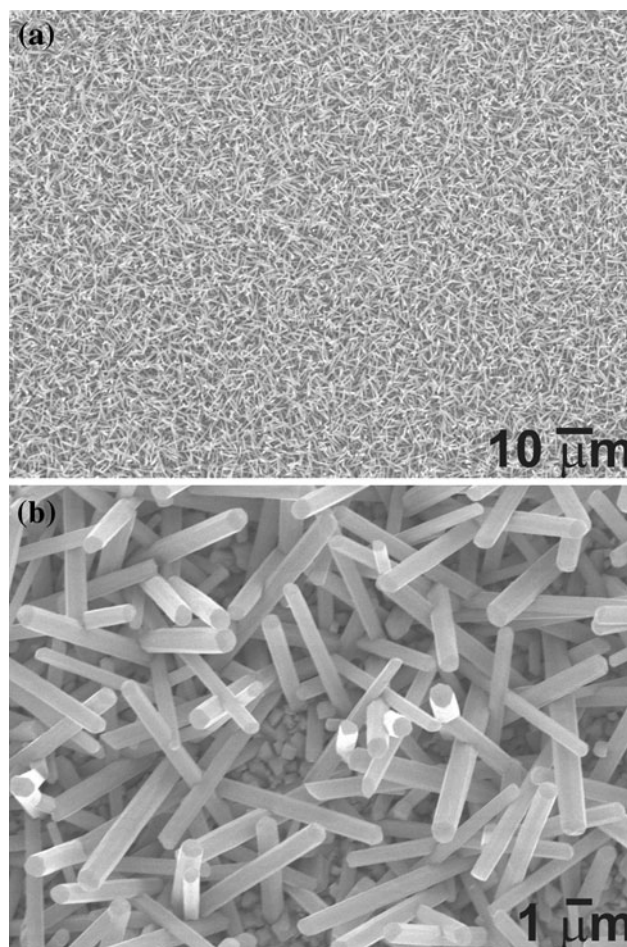


**Fig. 2** SEM images of $RuO_2$ nanorods synthesized with 100 sccm of $O_2$ at 1000 °C for 5 h under the working pressure of 3 torr shown at **a** low- and **b** high-magnification

clear relationship between the density of the $RuO_2$ rods and the $O_2$ flow rate was not observed due to the limited data. Apparently, further experiments at more fine tuned $O_2$ flow rates need to be performed to reveal how exactly the density of $RuO_2$ rods changes with the $O_2$ flow rate. It is also noted that some of the club-like and hollow rods have shorter length and smaller width as indicated by arrows in Fig. 3b, d, and f. It is expected that the initial size of the $RuO_2$ rods are determined by the size of the gold catalyst particles. Bigger catalyst particles will grow bigger $RuO_2$ rods while smaller catalyst particles will grow smaller $RuO_2$ rods. During the growth of the $RuO_2$ rods, due to the oxygen favorable competition, the bigger $RuO_2$ rods will grow faster than the smaller $RuO_2$ rods. As a result, some smaller $RuO_2$ rods will exist in the array of bigger $RuO_2$ rods. The above results indicate that a low $O_2$ flow rate of 100 sccm was suitable for the synthesis of polygonal prism-like $RuO_2$ nanorods while the high $O_2$ flow rate in the range of 300–600 sccm resulted in the formation of club-shaped sub-micron size $RuO_2$ structures.
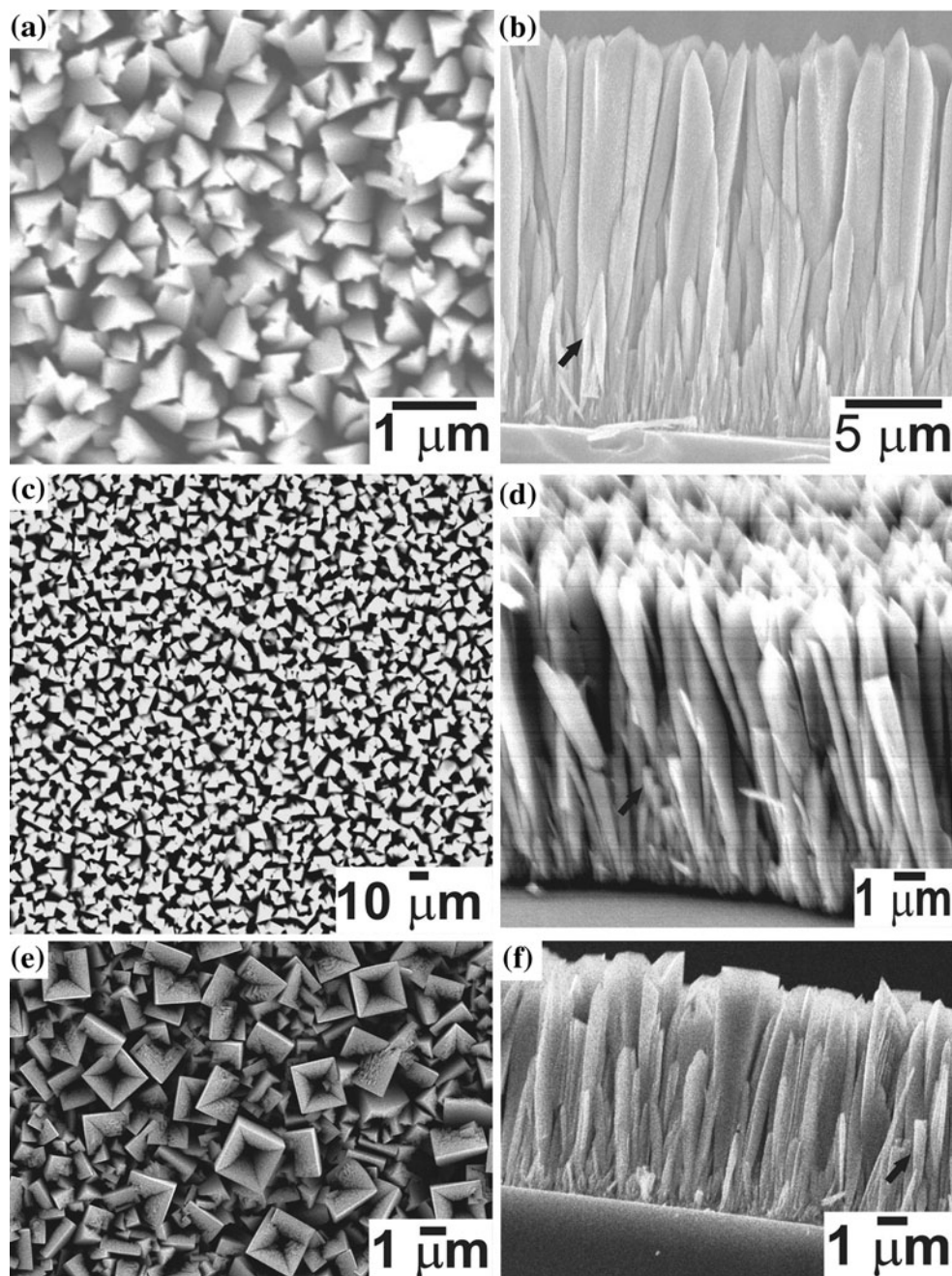
**Fig. 3** SEM images of club-like $RuO_2$ material produced at 1000 °C for 5 h at the pressure of 3 torr. **a** Top and **b** cross-sectional views of the $RuO_2$ structures formed at $O_2$ flow rate of 300 sccm. **c** Top and **d** cross-sectional views of the $RuO_2$ samples synthesized at $O_2$ flow rate of 600 sccm. **e** Top and **f** cross-sectional views of the $RuO_2$ material formed at $O_2$ flow rate of 1800 sccm

### Effect of working pressure on the formation of $RuO_2$ nanostructures

Further, the synthesis of $RuO_2$ was carried out at different working pressures to study their effect on the formation of the $RuO_2$ nanostructures. The top and cross-sectional views of $RuO_2$ nanostructures synthesized at working pressure of 380 torr (0.5 atm) are shown in Fig. 4a, b, respectively. The $O_2$ flow rate was maintained at 600 sccm at the synthesis

temperature of 1000 °C for 5 h. The SEM images reveal the growth of high density vertical nanorods which are 1.6 μm long and have an obelisk or a rectangular tip. In addition to these vertically grown nanorods, the sample also exhibits a pine tree-like growth (Fig. 4c) at the edges of the Si substrate. Figure 4d shows a typical SEM image of the pine tree-like nanostructures synthesized at 760 torr (1.0 atm) for 5 h with 600 sccm of $O_2$. The pine tree-like structure consists of a vertical trunk with horizontal branches which are
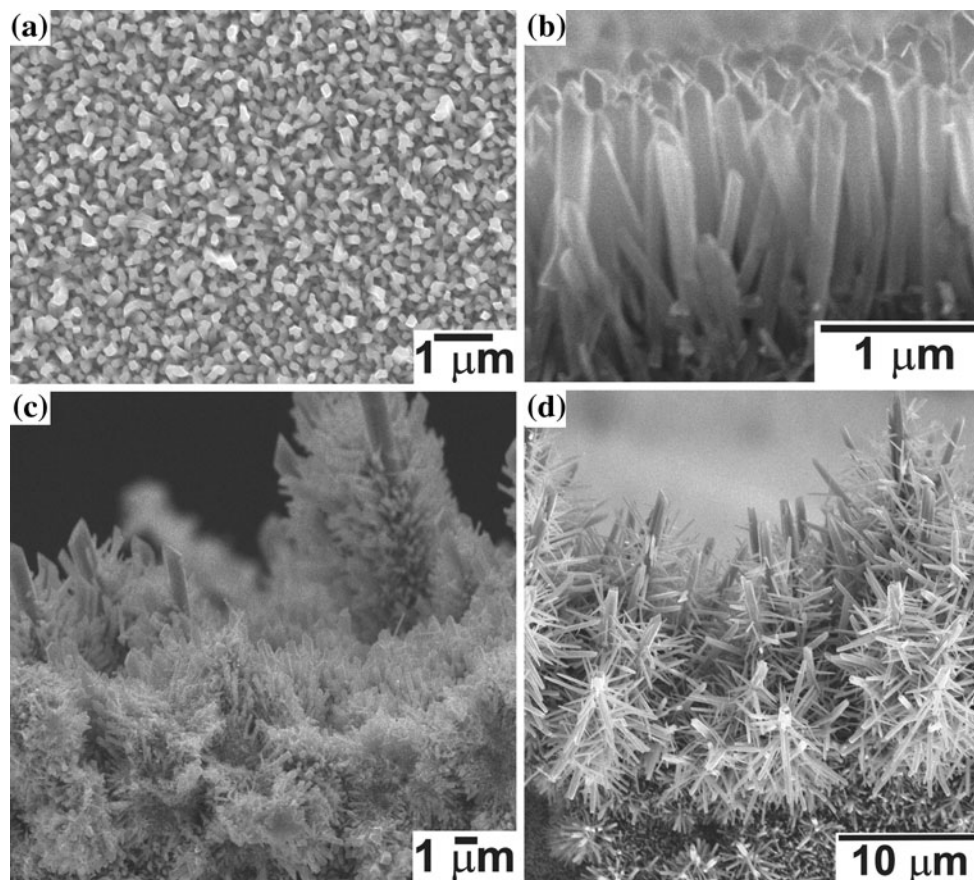
**Fig. 4 a** Top view and **b** cross-sectional view SEM images of the RuO$_2$ nanostructures synthesized at pressure of 380 torr of 600 sccm O$_2$ flow at 1000 °C. **c** Pine tree-like RuO$_2$ nanostructures formed at the edge of the Si substrate under the same synthesis conditions. **d** Pine tree-like RuO$_2$ nanostructures grown at the pressure of 760 torr with 600 sccm of O$_2$

perpendicular to the trunk and the neighboring branches distribute around the trunk in a helical staircase fashion. A particular trunk in Fig. 4d grows to a height of 13 μm with branches as long as 5 μm. The reason of the pine tree-like growth of RuO$_2$ at the Si edge can be understood as follows. The gold film is coated on Si surface by simple sputtering technique. However, the deposition of gold catalyst layer on Si is not perfectly uniform. Since the deposition is performed at room temperature, there exists no strong adhesion between Si surface and gold layer. During the synthesis, the flow of the reaction vapor is expected to drag the nucleated gold nanoparticles to the downstream end of the Si surface due to the large working pressure (380 and 760 torr) and high O$_2$ flow rate of 600 sccm. Hence, the large density and inhomogeneous dispersion of gold particles on downstream end of Si surface will facilitate the pine tree-like growth of RuO$_2$.

To the best of the authors' knowledge, these pine tree-like structures have not been reported earlier for RuO$_2$. However, similar structures have been reported for PbS [23], ZnO [24], and InAs [25]. The mechanism of pine tree-like growth observed in PbS [23] has been attributed to the dislocations in the crystal structure. The screw dislocations

along the length of nanorods provide spiral growth points favorable to the branched crystal growth. It was also suggested that the nanowire trunks in the pine trees are driven by dislocation, whereas the branches of the pine trees (and the hyperbranched nanowires) grow via a slower VLS process [23]. Besides PbS, the dislocation-driven nanowire growth mechanism is expected to occur in materials that are prone to have screw dislocations, such as SiC, GaN, ZnO, and CdS, which are fabricated both in vapor- and solution-phase growth. The presence of screw dislocations in the trunks of pine tree structures was confirmed in PbS using diffraction contrast TEM under the strong two-beam conditions [26]. The pine tree-like growth mechanism in ZnO [24] has been attributed to the mismatch between the planes of the branch and the planes of the trunk. In view of the growth model proposed for the pine tree structures of PbS [23], the dislocation-driven nanowire growth mechanism is also expected to be responsible for the pine tree-like structures of RuO$_2$. Moreover, when the supersaturation of RuO$_2$ vapor is slow, the growth along the crystalline side walls is suppressed resulting in a one-dimensional growth. As suggested for PbS [23], diffraction contrast TEM is a

powerful technique to image dislocations in crystals that relies on additional electron diffraction due to the bending of atomic planes near the dislocation core. Hence, to find the exact growth mechanism of the pine tree-like $RuO_2$ structure, TEM examinations on $RuO_2$ structure with pine tree-like morphology is necessary. The pine tree-like growth was not observed in the samples synthesized at $O_2$ flow rate of 600 sccm and pressure of 3 torr (see the corresponding SEM image of Fig. 3d). In conclusion, the high working pressure results in the formation of pine tree-like hierarchical $RuO_2$ nanostructures, while the low working pressure suppresses the growth along radial directions and is favorable for the formation of club-like structures with an obelisk tip at the $O_2$ flow rate of 600 sccm.

### Effect of Ar/O₂ concentration ratio on the formation of RuO₂ nanorods

To study the effect of $O_2$ concentration on the formation of $RuO_2$ nanostructure, $O_2$ was diluted with Ar gas to obtain various Ar/$O_2$ concentration ratios, while the total flow rate of $O_2$ and Ar was set constant at 600 sccm. Figure 5a–c shows the SEM images of $RuO_2$ nanostructures synthesized at $O_2$ and Ar flow rates of 30 and 570 sccm (5 vol.% $O_2$), 60 and 540 sccm (10 vol.% $O_2$), and 150 and 450 sccm (25 vol.% $O_2$), respectively, at 1000 °C and working pressure of 3 torr for 5 h. The cross-sectional SEM images in Fig. 5a–c show only the formation of dense club-like submicron vertically aligned $RuO_2$ rods with obelisk tips under all the synthesis conditions. The club-like rods synthesized at 5 vol.% $O_2$ (Fig. 5a) and 10 vol.% $O_2$ (Fig. 5b) concentrations have an average length of 2.2 μm. The average length of the $RuO_2$ nanorods increases to 2.5 μm at 25 vol.% $O_2$ concentration (Fig. 5c) and grows up to 10 μm at 100 vol.% $O_2$ concentration (see the corresponding SEM image in Fig. 3d). The increase in length of the nanorods with an increase in the concentration of $O_2$ can be attributed to the higher proportion of $O_2$ in the gas mixture. An increase in $O_2$ concentration results in the formation and transportation of the greater amount of
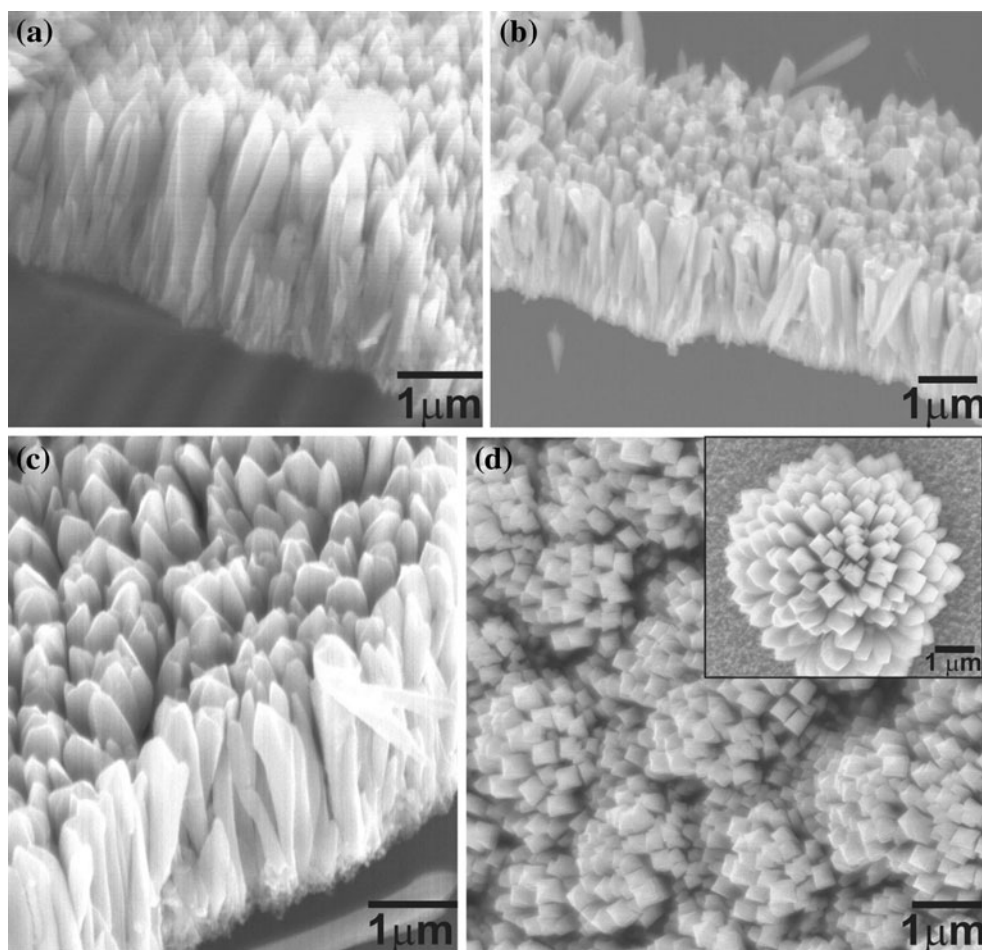


**Fig. 5** SEM images of $RuO_2$ formed with different Ar/$O_2$ mixture concentration of **a** 5 vol.% $O_2$, **b** 10 vol.% $O_2$, and **c** 25 vol.% $O_2$, with the total flow rate of $O_2$ and Ar fixed at 600 sccm. **d** SEM image of $RuO_2$ flower-like structures formed at 5 vol.% $O_2$ at the edge of Si substrate. *Inset* of **d** shows single flower-like structure

volatile oxides of Ru which contribute towards an increased length of $RuO_2$ nanorods. In other words, the length of nanorods synthesized in the presence of mixture of $O_2$ and Ar gas decreases with the increase of the concentration of Ar gas in the mixture. This result indicates that $O_2$ is far more effective than Ar for the synthesis of $RuO_2$ nanorods. Similar to the $RuO_2$ nanorods synthesized at different $O_2$ flow rates, some of the $RuO_2$ nanorods synthesized at different ratios of $O_2$/Ar also have smaller dimensions than the majority of the nanorods. In addition to the regular club-like structures formed at 5 vol.% $O_2$, patches of very high density flower-like structures were also observed at the edge of the Si substrate (Fig. 5d). These flower-like structures have width between 1 and 6 μm and are composed of short nanorods of width around 300 nm. The surface of these nanorods is very smooth and well faceted. The inset in Fig. 5d shows a single flower-like structure of about 6 μm wide. The high supersaturation of $RuO_2$ facilitated the homogenous nucleation throughout the Si substrate. Moreover, the slow reaction due to the small concentration of $O_2$ allowed a large bundle of nanorods to grow up from a central nucleus giving rise to the flower-like growth. The flower-like structures were not observed on the samples synthesized at the $O_2$ concentrations of 10 or 25 vol.%. However, the flower-like structures are more commonly observed in ZnO materials [27, 28].

### Structural analysis by transmission electron microscopy

Figure 6a shows the TEM image of the top portion of a club-like nanorod synthesized at the $O_2$ flow rate of 300 sccm at the pressure of 3 torr (the corresponding SEM images are shown in Fig. 3a–b). The TEM image clearly depicts the faceted surface of a 350 nm wide nanorod with an obelisk tip. The HRTEM image (Fig. 6 b) shows the equally spaced lattice fringes along the nanorod. The inset of Fig. 6b shows the magnified view of the region marked by the open box in Fig. 6b. The lattice fringes are separated by a distance of 0.336 nm which corresponds to the interplanar distance of (110) plane of rutile tetragonal $RuO_2$ crystal. Figure 6c shows the TEM image of the $RuO_2$ nanorods synthesized at 30 sccm of $O_2$ (5 vol.% $O_2$) and 570 sccm of Ar at 3 torr (see the corresponding SEM image in Fig. 5a). The tiny nanorods are stacked together to form bundle. Figure 6d shows the HRTEM image of the nanorods in the region marked by an open circle in Fig. 6c. The HRTEM image shows the equally spaced lattice fringes separated by 0.332 nm which corresponds to the interplanar distance of (110) plane of rutile tetragonal $RuO_2$ suggesting the growth along [001] direction. The SAED spot patterns of nanorods shown in Fig. 6a and c are presented in Fig. 6e and f, respectively. HRTEM images

with equally spaced lattice fringes and SAED patterns with clear bright spots confirm the high purity and crystalline nature of the as-synthesized nanorods.

### Theoretical consideration

Rutile $RuO_2$ crystal is fairly stable. Ruthenium is in nominally +4 state and oxygen in −2 state. The cohesive energy is mostly due to oxygen's planer $sp^2$ hybridization and ruthenium's 5s4d hybridization. Each oxygen atom has three co-planar Ru neighbors, and each Ru atom is at the center of a slightly deformed octahedron cage formed by six oxygen atoms. The Ru–O bond length in [110] direction is only 2% shorter than the other Ru–O bonds. These structure characteristics considerations show that the individual $RuO_2$ molecule has a higher energy and hence cannot be a major species in the chemical vapor. It is well known that one must use $O_2$ to form chemical vapor of $RuO_3$ and $RuO_4$ for transporting Ru to the growth site.

Standard density functional theory for quantum chemistry [29] is used to study the energy and stable structures of molecular ruthenium oxides. The local density approximation [30] is used for the exchange–correlation energy. The electronic structure and total energies are obtained using the first-principle self-consistent calculation. A linear combination of atomic orbitals of Gaussian type centered on each atom is used to expand the electronic wavefunction [31, 32]. Three s-type and two p-type orbitals are used for each oxygen atom, while nine s-type, eight p-type, and one d-type orbital are used for each Ru atom. This set-up results in 57 basis orbitals for each $RuO_2$ unit. All structure parameters (bond lengths and bond angles) are fully relaxed until residual forces are less than $10^{-5}$ Hartree/ Angstrom.

The electronic structure calculation confirms that $RuO_2$ is higher in energy compared to $RuO_3$ and $RuO_4$. Because of the $sp^2$ wavefunction of the oxygen, the stable structure of $RuO_2$ is not linear but forms O–Ru–O angle at 150°. Calculation also shows that the stable structure of both $RuO_3$ and $RuO_4$ are non-planar, due to the three-dimensional nature of ruthenium's d-wavefunction. From the calculation it can be concluded that $2RuO_2 + O_2 \rightarrow 2RuO_3$ has an energy gain of 3.4 eV per Ru, and $RuO_2 + O_2 \rightarrow RuO_4$ has a larger energy gain of 6.7 eV per Ru. The structure calculation also suggests that the less stable $RuO_3$ (as compared to $RuO_4$) may be more suitable for nanorods growth, because the exposed ruthenium d-orbitals of $RuO_3$ are ready to bond to oxygen's $sp^2$ to form a crystal. Clearly the source temperature will influence greatly the relative concentration of $RuO_3$ and $RuO_4$ in the chemical vapor. Previous study [33] reported that at the synthesis temperature above 1000 °C, formation of $RuO_4$ would dominate. It is desirable to directly investigate the
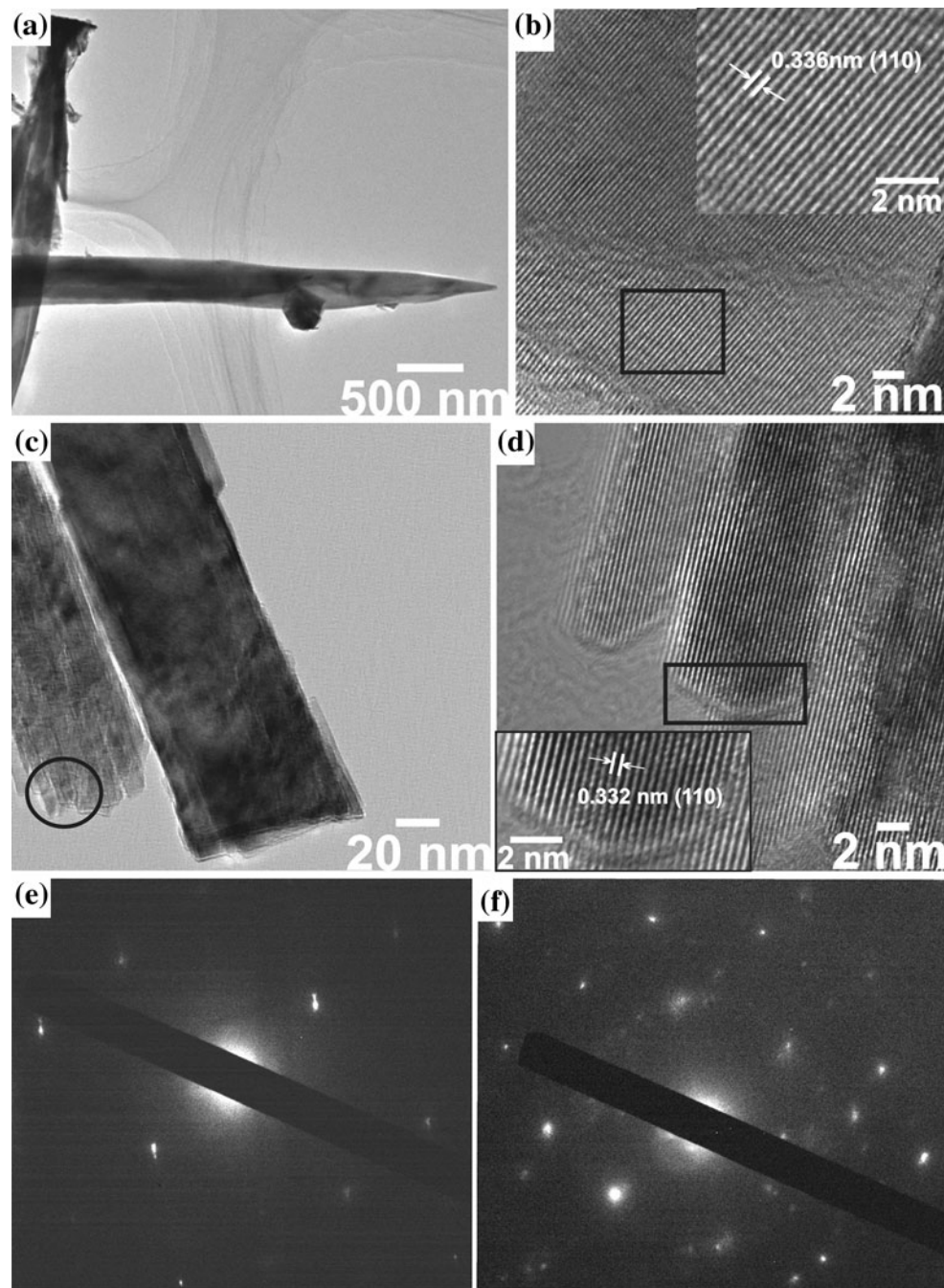
**Fig. 6** TEM images of RuO$_2$ nanorods. **a** TEM image of the top portion of a club-like RuO$_2$ nanorod with an obelisk tip synthesized at 300 sccm of O$_2$ at pressure of 3 torr. **b** HRTEM image of the club-like nanorod. The *inset* shows the magnified view of the region marked by the *open box* in **b** showing the clear lattice fringes separated by a distance of 0.336 nm, which can be assigned to the interplanar distance corresponding to the (110) planes. **c** High-magnification TEM image of the nanorods grown at the pressure of 3 torr with the O$_2$ flow of 30 sccm and Ar flow of 570 sccm. **d** HRTEM image of the region marked by the *open circle* in **c**. The inset is the enlarged view of the region marked by the open box in **d** indicating the clear lattice fringes separated by 0.336 nm which can be attributed to the interplanar distance corresponding to the (110) planes. **e** and **f** SAED patterns of the club-like nanorods shown in **a** and **c**, respectively

relative concentration of RuO$_3$ and RuO$_4$ in the chemical vapor under different growth conditions.

The calculation also indicates that the rich O$_2$ environment at the Ru source is the preferable condition to grow

Ru nanorods because it will promote the formation of RuO$_3$ and RuO$_4$ in the chemical vapor. However, one needs somewhat lower oxygen partial pressure at the growth site so that RuO$_3$ and RuO$_4$ can form RuO$_2$ crystal

and release $O_2$. Our experiments have shown that more uniform nanorods with less branching and/or tree shape growth are obtained using various mixtures of $O_2$ and Ar. In the future, we plan to use a separate source chamber under higher $O_2$ pressure, and then inject the chemical vapor into the growth tube under continuous Ar flow to gain a better control of the growth of the crystalline $RuO_2$ nanorods.

## Conclusions

In summary, highly crystalline $RuO_2$ nanorods were synthesized by thermal evaporation of $RuO_2$ powder using gold as catalyst on silicon substrate. The $O_2$ flow rate, concentration, and working pressure play significant roles in the formation of $RuO_2$ nanostructures. Polygonal prisms with uniform width along the length were synthesized at the $O_2$ flow rate of 100 sccm, while club-like micron-sized vertically aligned nanorods with obelisk tips were synthesized at increased $O_2$ flow rates of 300 and 600 sccm. High flow rate of 1800 sccm of $O_2$ results in the formation of sub-micron size hollow rods with square-shaped tips. Low working pressure results in the formation of linear nanorods, while high working pressures result in both vertically aligned nanorods and pine tree-like branched hierarchical $RuO_2$ nanostructures. The formation of pine tree-like hierarchical $RuO_2$ nanostructures can be attributed to the screw dislocation or lattice mismatch. The experimental results indicate that the decrease of $O_2$ concentrations in the $Ar/O_2$ mixtures with the total flow rate of 600 sccm suppresses the growth speed of the $RuO_2$ nanorods. A flower-like pattern consisting of short $RuO_2$ nanorods was also observed in the sample synthesized at the $O_2$ concentration of 5 vol.%. The as-synthesized $RuO_2$ nanostructures with obelisk tips can find applications in field emitters due to their unique morphology.

## References

1. Xu JH, Jarlborg T, Freeman AJ (1989) Phys Rev B 40:7939
2. Ryden WD, Lawson AW, Sartian CC (1970) Phys Rev B 1:1494
3. Green ML, Gross ME, Papa LE, Schnoes KJ, Brasen D (1985) J Electrochem Soc 132:2677
4. Khanna PK, Bhatnagar SK, Sisodia ML (1988) J Phys D 21:1796
5. Dziedzic A, Golonka LJ, Kozlowski J, Licznerski BW, Nitsch K (1997) Meas Sci Technol 8:78
6. Kim IH, Kim KB (2001) Electrochem Solid State Lett 4:A62
7. Park BO, Lokhande CD, Park HS, Jung KD, Joo OS (2004) J Mater Sci 39:4313. doi:10.1023/B:JMSC.0000033415.47096.db
8. Norga GJ, Fe L, Wouters DJ, Maes HE (2000) Appl Phys Lett 76:1318
9. Hartmann AJ, Neilson M, Lamb RN, Watanabe K, Scott JF (2000) Appl Phys A 70:239
10. Kuhn AT, Mortimer CJ (1973) J Electrochem Soc 120:231
11. Ferro S, De Battisti A (2002) J Phys Chem B 106:2249
12. Lister TE, Tolmachev YV, Chu Y, Cullen WG, You H, Yonco R, Nagy Z (2003) J Electroanal Chem 554:71
13. Ryan JV, Berry AD, Anderson ML, Long JW, Stroud RM, Cepak VM, Browning VM, Rolison DR, Merzbacher CI (2000) Nature 406:169
14. Hsieh CS, Tsai DS, Chen RS, Huang YS (2004) Appl Phys Lett 85:3860
15. Delmer O, Balaya P, Kienle L, Maier J (2008) Adv Mater 20:501
16. Iembo A, Fuso F, Arimondo E, Ciofi C, Pennelli G, Curro GM, Neri F, Allegrini M (1997) J Mater Res 12:1433
17. Kim IH, Kim KB (2004) J Electrochem Soc 151:E7
18. Satishkumar BC, Govindaraj A, Nath M, Rao CNR (2000) J Mater Chem 10:2115
19. Cheng KW, Lin YT, Chen CY, Hsiung CP, Gan JY, Yeh JW, Hsieh CH, Chou LJ (2006) Appl Phys Lett 88:043115
20. Chen RS, Chen CC, Huang YS, Chia CT, Chen HP, Tsai DS, Tiong KK (2004) Solid State Commun 131:349
21. Liu YL, Wu ZY, Lin KJ, Huang JJ, Chen FR, Kai JJ, Lin YH, Jian WB, Lin JJ (2007) Appl Phys Lett 90:013105
22. Vetrone J, Foster CM, Bai GR, Wang A, Patel J, Wu X (1998) J Mater Res 13:2281
23. Bierman MJ, Lau YKA, Kvit AV, Schmitt AL, Jin S (2008) Science 320:1060
24. Zhao FH, Li XY, Zheng JG, Yang XF, Zhao FL, Wong KS, Wang J, Lin WJ, Wu MM, Su Q (2008) Chem Mater 20:1197
25. May SJ, Zheng JG, Wessels BW, Lauhon LJ (2005) Adv Mater 17:598
26. Williams DB, Carter CB (1996) Transmission electron microscopy: a textbook for materials science. Plenum, New York
27. Wang Z, Qian XF, Yin J, Zhu ZK (2004) Langmuir 20:3441
28. Zhang H, Yang D, Ma XY, Ji YJ, Xu J, Que DL (2004) Nanotechnology 15:622
29. Jones RO, Gunnarsson O (1989) Rev Mod Phys 61:689
30. Ceperley DM, Alder BJ (1980) Phys Rev Lett 45:566
31. Ditchfield WJH, Pople JA (1971) J Chem Phys 54:724
32. Hariharan PC, Pople JA (1973) Theor Chim Acta 28:213
33. Bell WE, Tagami M (1963) J Phys Chem 67:2432